Quantum site percolation on triangular lattice and the integer quantum Hall effect

V. V. Mkhitaryan and M. E. Raikh
Department of Physics, University of Utah, Salt Lake City, UT 84112
(Received 22 November 2008; revised manuscript received 24 January 2009; published 3 March 2009)

Generic *classical* electron motion in a strong perpendicular magnetic field and random potential reduces to the *bond* percolation on a *square* lattice. Here we point out that for certain smooth two-dimensional potentials with 120° rotational symmetry this problem reduces to the *site* percolation on a *triangular* lattice. We use this observation to develop an approximate analytical description of the integer quantum Hall transition. For this purpose we devise a quantum generalization of the real-space renormalization group (RG) treatment of the site percolation on the triangular lattice. In quantum case, the RG transformation describes the evolution of the *distribution* of the 3×3 scattering matrices at the sites. We find the fixed point of this distribution and use it to determine the critical exponent, ν, for which we find the value $\nu\approx 2.3\div 2.76$. The RG step involves only a *single* Hikami box and thus can serve as a minimal RG description of the quantum Hall transition.

DOI: 10.1103/PhysRevB.79.125401 PACS number(s): 72.15.Rn, 73.20.Fz, 73.43.−f

I. INTRODUCTION

Network-model formulation of the Anderson localization problem was first introduced in Ref. 1. The key observation made in Ref. 1 is that a complex motion of electron in disorder potential can be reduced to the motion along the links of the network (in both directions) with disorder incorporated via random phases of scattering from the nodes of the network. Since then, the network-model approach became a powerful tool for numerical studies of disordered systems. In these studies the randomness is incorporated into the phases accumulated along the network links. A great advantage of the network-model approach to localization is that it can be conveniently applied to various universality classes[2] of disorder. In order to capture the specifics of a given class, one has to impose appropriate symmetry requirements on the random phases on the links, which fixes the form of S matrix at the nodes. This is achieved by introduction of an internal space associated with the link of the network model, which possesses a desired symmetry. For example,[3] with two-component links (one component for one spin projection) for each direction of propagation the requirements of unitarity and time-reversal symmetry allowed to reveal a delocalization transition expected in two-dimensional (2D) systems with spin-orbit scattering. Comprehensive review of the results obtained with the help of the network model is given in Ref. 5. In addition to establishing the existence of localization transitions in different classes, numerical simulations of the network models with the help of transfer-matrix method yield quantitative characteristics of the critical point. These characteristics include critical exponent, critical level statistics, and critical conductance distribution. Corresponding references can be found in the review of Ref. 5. Note that, with the exception of Ref. 4 where a particular two-channel network model was considered for arbitrary graph, the underlying network in all previous studies was a square lattice.

Especially convenient for modeling with a network is the *chiral* motion of a 2D electron in a disorder potential and a strong perpendicular magnetic field. This is because the corresponding network is *directed*. Directed character of the network with chiral scattering at the nodes allowed Chalker and Coddington[6] to demonstrate conclusively that there is only a single delocalized state per Landau level. This finding is of great importance since it is the underlying reason for sharp conductivity peaks at the quantum Hall transition.

On physical grounds, the seminal Chalker-Coddington (CC) model[6] of the integer quantum Hall transition can be introduced in a natural way with the help of a two-dimensional potential,

$$U(x,y)=\cos(\pi x)\cos(\pi y). \tag{1}$$

In this potential, the equipotential lines $U(x,y)=0$ form a square lattice. For any nonzero ε equipotentials $U(x,y)=\varepsilon$ are closed. For positive ε these equipotentials encircle the maxima $(x,y)=(2m,2n)$ [and also $(2m+1,2n+1)$] of $U(x,y)$, while for $\varepsilon<0$ equipotentials encircle the minima $(x,y)=(2m,2n+1)$ [and $(2m+1,2n)$] of $U(x,y)$. In a strong perpendicular magnetic field 2D electron drifts along equipotentials. Then reconfiguration of equipotentials at $\varepsilon=0$, as illustrated in Fig. 1(a), manifests the change in the character of motion.

Chalker and Coddington[6] captured the quantum character of motion in $U(x,y)$ by assigning to the saddle points at $(x_m,y_n)=(m-\frac{1}{2},n-\frac{1}{2})$ where the potential behaves as

$$U(x-x_m,y-y_n)\approx(-1)^{m+n}\pi^2(x-x_m)(y-y_n)$$
$$=(-1)^{m+n}\frac{\pi^2\rho^2}{2}\sin 2\varphi, \tag{2}$$

a scattering matrix

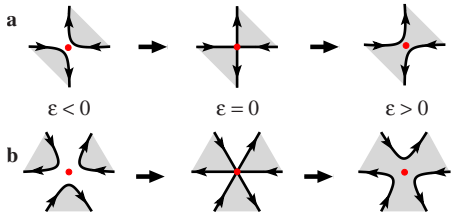

FIG. 1. (Color online) (a) Evolution of equipotentials near the saddle point of potential (1) as the energy ε crosses over from $\varepsilon<0$ to $\varepsilon>0$; (b) evolution of equipotentials near the nodes of potential (4) with ε. Three equipotential lines touch at $\varepsilon=0$.

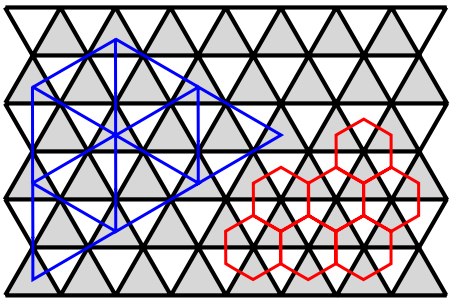

FIG. 2. (Color online) Equipotential lines $\varepsilon=0$ of potential (4) constitute a triangular lattice. Minima of $W(x,y)$ are in the centers of shaded triangles. Blue lines constitute a triangular lattice of supersites with lattice constant, $\sqrt{3}$. Red lines: hexagonal lattice with sites in the centers of triangles. Each site of a triangular lattice is surrounded by a hexagon.

$$S_{cc}(\varepsilon)=\begin{pmatrix} \frac{1}{\sqrt{2}}+\varepsilon & \frac{1}{\sqrt{2}}-\varepsilon \\ -\frac{1}{\sqrt{2}}+\varepsilon & \frac{1}{\sqrt{2}}+\varepsilon \end{pmatrix}. \tag{3}$$

Here ρ and φ are the polar coordinates with origin at (x_m,y_n), and ε is the dimensionless energy. For a realistic potential with magnitude, U_0, and correlation length, d, dimensionless energy, ε, is the physical energy measured in the units of the width, $\Gamma\sim U_0 l^2/d^2$, where l is the magnetic length. Chalker and Coddington[6] demonstrated that, in order to account for a smooth disorder, it is sufficient to assume that the phases, acquired by a drifting electron between the saddle points, are random.

In this paper we show that the description of the quantum Hall transition can also be obtained based on the potential

$$W(x,y)=\sum_{n,m} V(\mathbf{r}-n\mathbf{e}_1-m\mathbf{e}_2), \tag{4}$$

which has a *triangular* symmetry, i.e., $\mathbf{e}_1=(1,0)$ and $\mathbf{e}_2=(1/2,\sqrt{3}/2)$ are the basis unit vectors of a triangular lattice; the function V is defined inside a "black half" of the rhombus-shape unit cell (see Fig. 2) in the following way:

$$V(\rho,\varphi)=\left[\rho\cos\left(\varphi-\frac{\pi}{6}\right)-\frac{1}{2\sqrt{3}}\right]\left[\rho\cos\left(\varphi-\frac{5\pi}{6}\right)-\frac{1}{2\sqrt{3}}\right]\times\left[\rho\cos\left(\varphi-\frac{3\pi}{2}\right)-\frac{1}{2\sqrt{3}}\right]. \tag{5}$$

Here ρ and φ are the polar coordinates with respect to the origin at $(\mathbf{e}_1+\mathbf{e}_2)/3$. The form of potential in the "white half" of a unit cell is given by Eq. (4) upon replacement $V(\rho,\varphi)\rightarrow -V(\rho,\varphi-\pi/3)$ and shifting the origin to the center of the white triangle.

Equipotentials of Eq. (5) evolve, as ε passes through 0, in a fashion *qualitatively different* from the case of quadratic symmetry. As shown in Fig. 1(a), in the case of quadratic symmetry, black regions (minima) get connected, while adjacent white regions (maxima) get disconnected. In contrast,

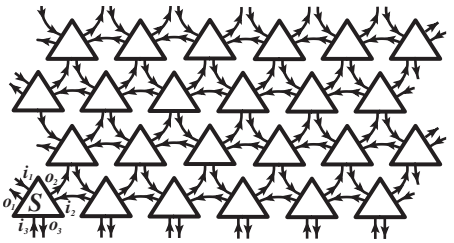

FIG. 3. Network model on a triangular lattice is illustrated. Three links enter a node, and three links exit each node; the nodes with S matrices [Eq. (7)] are depicted as triangles.

the behavior of the potential $W(x,y)$ near the nodes at $\mathbf{r}_{m,n}=(m-1/3)\mathbf{e}_1+(n-1/3)\mathbf{e}_2$ is given by

$$W(\rho,\varphi)=-\rho^2\sum_{q=0}^{\infty} c_q \sin[3(2q+1)\varphi], \tag{6}$$

where $c_q=\frac{2\sqrt{3}}{\pi}\{(2q+1)[9(2q+1)^2-4]\}^{-1}$. Corresponding evolution of equipotentials is illustrated in Fig. 1(b). We see that, as ε crosses zero, *three* black regions get joined at $\varepsilon=0$ *simultaneously*. This suggests that quantum-mechanical description of motion in the potential $W(x,y)$ requires, in addition to random phases on the links, introduction of a 3×3 scattering matrix at each node. Below we argue that the form of this matrix is

$$S_{\Delta}(\varepsilon)=\begin{pmatrix} \frac{2}{3}(1+\varepsilon) & -\frac{1}{3} & \frac{2}{3}(1-\varepsilon) \\ \frac{2}{3}(1-\varepsilon) & \frac{2}{3}(1+\varepsilon) & -\frac{1}{3} \\ -\frac{1}{3} & \frac{2}{3}(1-\varepsilon) & \frac{2}{3}(1+\varepsilon) \end{pmatrix}. \tag{7}$$

With matrices [Eq. (7)] in the nodes, the corresponding network model is shown in Fig. 3. In this network the phases on the links are random, as in Chalker-Coddington model, while all S matrices in the nodes [Eq. (7)] are the same. As we demonstrate in the present paper, this model can be treated numerically using the same MacKinnon-Kramer finite-size scaling algorithm[7] that was employed in Ref. 6 (for subsequent numerical studies of the Chalker-Coddington model see Refs. 8–20 and review articles[5,21]).

Chalker-Coddington model can be viewed as quantum version of the classical *bond* percolation. Establishing one-to-one correspondence between the classical bonds and the links is possible due to directed character of the chiral CC network. On the other hand, it was demonstrated in Ref. 22 that a simple real-space renormalization group (RG) procedure, based on decimation, leads to the closed equation for the classical bond percolation threshold. This procedure reproduces the exact threshold value and yields a very accurate estimate for the critical exponent. In Refs. 23–27 the classical RG procedure[22] was generalized to the quantum bond percolation. It was shown that corresponding integral RG equation yields, in addition to the accurate value of the quan-

tum critical exponent, a very accurate distribution of the critical conductance. A real-space RG procedure for a *site* percolation was proposed in the same paper.[22] This procedure is simpler than for the bond percolation and yields more accurate results. In the present paper this procedure is extended to the quantum case, where it describes the critical behavior of the directed network (Fig. 3). As in the classical case, the quantum RG analysis of on the triangular lattice is much easier than the quantum RG analysis of the Chalker-Coddington on the square lattice. This analysis is presented in Secs. II–V.

II. RG PROCEDURE FOR CLASSICAL PERCOLATION ON A TRIANGULAR NETWORK

In order to develop the RG description, it is necessary to incorporate disorder into the S matrices. The reason is that at each RG step three S matrices, connected by the links, are combined into one *super-S* matrix. Then the randomness in phases translates into the randomness of the elements of super-S matrix. A natural way to devise the quantum RG description is to start from a classical problem of electron drift along the sides of triangles (Fig. 2).

A. Classical drift on triangular lattice

Assume that the potential $W(x,y)$ is perturbed near the nodes as

$$W(\rho,\phi) = V_0 - c_0\rho^2 \sin(3\varphi) - c_1\rho^2 \sin(9\varphi) - \cdots, \quad (8)$$

where the random shift, V_0, is much smaller than 1 but much bigger than the "quantum" energy width, Γ. Depending on the shift, an electron drifting along equipotential $W=\varepsilon$ toward a node turns either to the left ($V_0<\varepsilon$) or to the right ($V_0>\varepsilon$) [see Fig. 1(b)]. We can conventionally call the nodes with $V_0<\varepsilon$ and $V_0>\varepsilon$ as "black" and "white" lattice sites, respectively. It is obvious that when the average, $\langle V_0\rangle$, is zero, the percolation threshold in potential (8) is $\varepsilon=0$. In the language of sites, the same is to say that 50% of sites are black at $\varepsilon=0$. It is, in fact, well known[28] that the exact threshold for site percolation on a triangular lattice is 50%. However, it is much less obvious that there is *complete equivalence* between the electron drift in potential (8) and the site percolation on a triangular lattice. Superficially, this can be seen from the fact that when two neighboring sites are black, they are connected via the black region. Still, rigorous proof requires additional steps, in particular, introducing auxiliary hexagons (see Fig. 2). This proof is given in Appendix A.

B. Classical RG scheme

The above mapping on the percolation problem allows one to employ the RG approach to the site percolation on triangular lattice put forward in Ref. 22. This procedure is much simpler than the RG for the bond percolation on the square lattice, proposed in the same paper. Note in passing that the bond percolation on the square lattice is the classical limit of the Chalker-Coddington model.[23]

As shown in Fig. 2, at each RG step[22] the lattice constant increases by a factor of $\sqrt{3}$. A site of a rescaled lattice, a *supersite*, is either black or white depending on the colors of the three constituting sites: if either *all three* or *only two* out of three constituting sites are black, then the supersite is black. Otherwise, the supersite is white. Quantitatively, the probability p' for a supersite to be black is expressed via the corresponding probability for the original site as

$$p' = R(p) = p^3 + 3p^2(1-p). \quad (9)$$

Fixed point, $p'=p=p_c$, of the transformation Eq. (9) reproduces the exact result $p_c=1/2$. Critical exponent is determined by the condition that the correlation radius, $\xi=(p-p_c)^{-\nu}$, on the original lattice is equal to the correlation radius $\sqrt{3}(p'-p_c)^{-\nu}$ on the renormalized lattice; i.e.,

$$\nu = \frac{\ln(\sqrt{3})}{\ln\left(\dfrac{dp'}{dp}\right)_{p=p_c}} = \frac{\ln(\sqrt{3})}{\ln(3/2)}. \quad (10)$$

Equation (10) yields $\nu=1.354$, which differs from the exact value, $\nu=4/3$, by only 1.6%.

The rationale behind transformation (9) is that the supersite is located in the center of the black cell in Fig. 2. Then the color of the supersite reflects the "percolation ability" of this black triangular cell so that even if one of the nodes constituting the vertices of the triangular cell is white, the cell still percolates "over black."

C. RG in the language of potential shifts

At this point we make an observation that the above RG procedure can be reformulated in the language of potential $W(x,y)$ with random shifts in the nodes, V_0. Namely, for V_0^1, V_0^2, and V_0^3 being the shifts at the nodes constituting a supernode, the shift V_0' of the supernode is defined as

$$V_0' = \mathrm{Mid}\{V_0^1, V_0^2, V_0^3\}, \quad (11)$$

where Mid stands for V_0 which is *smaller than maximal* but *larger than minimal* out of the three numbers. With V_0' defined by Eq. (11), RG equation (9) describes the evolution of probability that the shift exceeds ε.

The importance of the above observation is that reformulation of classical RG procedure in terms of potential shifts opens a possibility to capture the quantum-mechanical motion in the random potential. A prescription how to extend classical description to the quantum case is:[23] algorithm (11) should be cast in the form of a *scattering problem*.

III. REFORMULATION IN TERMS OF CLASSICAL TRANSMISSION

We identify the scattering object as a point where three equipotentials come close as shown in Fig. 4. Incident electron, i_1, either proceeds along the same equipotential into o_1 (reflection) or switches equipotentials and proceeds along o_2. Retention of equipotential (reflection) corresponds to positive $V_0-\varepsilon$ in the vertex, encircled in Fig. 4. In terms of scattering matrix

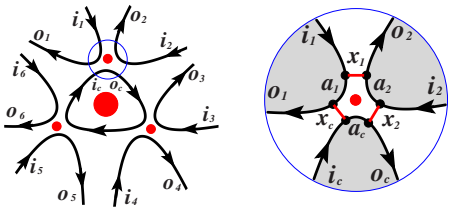

FIG. 4. (Color online) Left: superscattering object is shown with a big red dot, while constituting scattering objects are shown with small red dots. Right: detailed structure of the scattering object; black dots show the points of the close contact of equipotentials. Electron incident along equipotential, i, can either proceed along the same equipotential, a, or switch equipotential with probability $|x|^2$. The latter processes are illustrated with red dashes.

$$\begin{pmatrix} o_1 \\ o_2 \\ o_3 \end{pmatrix} = S \begin{pmatrix} i_1 \\ i_2 \\ i_3 \end{pmatrix}, \tag{12}$$

the same simple notion can be reformulated as follows. For positive $V_0-\varepsilon$, the matrix $S=S_+$ is a *unit matrix*, while for negative $V_0-\varepsilon$ the matrix $S=S_-$ has the form

$$S_- = \begin{pmatrix} 0 & 0 & 1 \\ 1 & 0 & 0 \\ 0 & 1 & 0 \end{pmatrix}.$$

Superscattering object consists of three scattering objects and is shown in the same figure.

Now we reformulate Eqs. (9) and (11) in yet another language of S matrices. Namely, the S matrix of a superscattering object is expressed via S matrices of constituting scattering objects upon reducing the number of legs from 12 to 6. We emphasize that this reduction can be carried out in two distinct ways, as illustrated in Fig. 5. The first way is to perform contractions as $o_2 \leftrightarrow i_2$, $o_4 \leftrightarrow i_4$, and $o_6 \leftrightarrow i_6$. The second variant of contractions is $o_2 \leftrightarrow i_1$, $o_4 \leftrightarrow i_3$, and $o_6 \leftrightarrow i_5$. Now it is straightforward to check that RG transformation (11) corresponds to the following rule for S matrix of the superscattering object, $\tilde{S}$. If the S matrices of either all three or only two of constituting objects are S_+, then $\tilde{S}=S_+$. In all other realizations, when at least two of constituting objects have the matrix S_-, we have $\tilde{S}=S_-$.

It is important to note that the above rule for $\tilde{S}$ applies

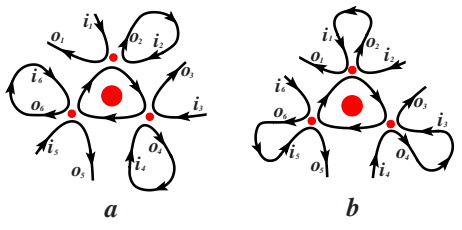

FIG. 5. (Color online) Two contributions to the kernel [Eq. (19)] originating from two variants of contraction of equipotentials are illustrated; (a) corresponds to $\tilde{x}^a$ [Eq. (16)], while (b) corresponds to $\tilde{x}^b$ [Eq. (17)].

independently of the way in which the contractions in Fig. 5 are performed. This is not the case in the quantum version to which we now turn.

IV. QUANTUM GENERALIZATION

Quantum S matrix of the scattering object differs from S_+ and S_- in two respects. First, at the points of close contact between each pair of equipotentials electron can switch equipotential *even for positive* $V_0-\varepsilon$, when it is forbidden classically. Corresponding classically forbidden transitions are illustrated in Fig. 4 with red (dark gray) dashes. Second, upon traveling between two subsequent points of close contact, electron accumulates the Aharonov-Bohm phase, ϕ_i. For example, the phase ϕ_1 is accumulated in course of drift between i_1 and o_1. These phases are irrelevant in the classical limit when the reflection amplitudes, y_i, are either 0 or 1. However, for intermediate $0<y_i<1$ the amplitude for an electron to execute a *close contour* around the center in Fig. 4 (following the red dashes in the clockwise direction) is *finite*. As a result, ϕ_i enter into quantum scattering matrix. Explicit form of S in terms of $0<y_i<1$ and ϕ_i can be obtained by solving three pairs of linear equations, describing quantum scattering at each of three points of the close contact of equipotentials. We have

$$S = \frac{-1}{1-x_1x_2x_3e^{i\psi}} \times \begin{pmatrix} y_1y_3e^{i\phi_1} & x_1y_2y_3e^{i(\phi_1+\phi_2)} & x_1x_2e^{i\psi}-x_3 \\ x_2x_3e^{i\psi}-x_1 & y_1y_2e^{i\phi_2} & y_1x_2y_3e^{i(\phi_2+\phi_3)} \\ y_1y_2x_3e^{i(\phi_1+\phi_3)} & x_1x_3e^{i\psi}-x_2 & y_2y_3e^{i\phi_3} \end{pmatrix}, \tag{13}$$

where $x_j=\sqrt{1-y_j^2}$ stand for the transmission amplitudes, and

$$\psi = \phi_1 + \phi_2 + \phi_3 \tag{14}$$

is the net phase accumulated along the closed contour. It is easy to check that matrix (13) is unitary. It is also straightforward to verify that in the classical limits, when *all* $x_j=0$ or $x_j=1$, Eq. (13) correctly reproduces S_+ and S_-, respectively. Detailed derivation of the form Eq. (13) of the scattering matrix is presented in Appendix B.

A. Form of the matrix S_Δ

From Eq. (13) we can establish the form of the scattering matrix $S_\Delta(\varepsilon)$ [Eq. (7)] with the help of the following duality argument. Due to triangular symmetry of the potential $\rho^2 \sin(3\varphi)$ we have $x_1=x_2=x_3=x$. Consider now the transition point, $\varepsilon=0$. At this point the probability for electron incident along, say, i_1 (see Fig. 4) to be deflected to the left (along o_1) is equal to the probability to be deflected to the right (along o_2). Less trivial is that the phase, ψ, must be zero at $\varepsilon=0$. This is the consequence of the fact that the scattering problems for electron with energy ε and $-\varepsilon$ are equivalent if we change the drift direction from clockwise to anticlockwise; this change implies also the change in the sign of ψ.

With $\psi=0$, the condition, $(1-x^2)^2=(x^2-x)^2$, of "equal deflection" to the left and to the right, yields a single physical root $x=-1/2$. Substituting it back in matrix (13) reduces it to scattering matrix (7) with $\varepsilon=0$. Then for probabilities $i_1 \to o_1$ and $i_1 \to o_2$ we get 4/9, while the probability $i_1 \to o_3$ is 1/9. Including small finite ε can be also performed with the help of the duality argument, namely, that the probability of deflection to the left with energy ε is equal to the probability of deflection to the right with energy $-\varepsilon$. On the other hand, the change in probability $i_1 \to o_3$ with ε is $\propto \varepsilon^2$. The role of the matrix S_Δ is central to the transfer-matrix treatment of the network model; see Appendix C.

B. Quantum RG equation

We now turn to the quantum RG procedure. In contrast to evolution of probability, p, upon rescaling of the lattice constant in the classical case, this procedure is formulated in terms of evolution of the *distribution function*, $Q(x)$, of the *absolute values* of the transmission amplitudes, x_i. Thus the quantum generalization of Eq. (9) at the step n is the following recurrence relation:

$$Q_{n+1}(x) = T[Q_n(x)] = \int \left[\prod_{j=1}^{3} dx_j Q_n(x_j) \right] K(x,x_1,x_2,x_3). \tag{15}$$

The kernel, K, represents the conditional probability that, after performing the contractions, the transmission coefficient $i_c \to o_1$ in Fig. 4 is equal to x, provided that the constituting transmission coefficients are x_1, x_2, and $x_c=x_3$, as illustrated in Fig. 4. In analytical evaluation of the dependence $x(x_1,x_2,x_3)$ it is important to take into account that this dependence is different for two variants of contractions. For a variant $o_2 \leftrightarrow i_2$, shown in Fig. 5(a), the transmission coefficient is given by

$$|\tilde{x}_c^a|^2 = 1 - \left| \frac{(\sqrt{1-x_1^2}e^{i\varphi} + \sqrt{1-x_2^2})\sqrt{1-x_3^2}}{(1-x_1x_2x_3e^{i\psi})e^{i\varphi} + \sqrt{(1-x_1^2)(1-x_2^2)}} \right|^2, \tag{16}$$

where φ is the phase along the contour (o_2,i_2), which is now *closed*. Correspondingly, for the second kind of closing $o_2 \leftrightarrow i_1$ [Fig. 5(b)], the transmission coefficient has the form

$$|\tilde{x}_c^b|^2 = 1 - \left| \frac{(x_1 - e^{i\varphi})\sqrt{(1-x_2^2)(1-x_3^2)}}{(1-x_1x_2x_3e^{i\psi})e^{i\varphi} + x_2x_3e^{i\psi} - x_1} \right|^2, \tag{17}$$

where φ stands for the phase along (o_2,i_1). For details of derivation of Eqs. (16) and (17) see Appendix B.

Relations (16) and (17) define also the dependencies $\tilde{x}_1^{a,b}(x_1,x_2,x_3)$ and $\tilde{x}_2^{a,b}(x_1,x_2,x_3)$. It is important that the central phase, ψ, is *common* for all three dependencies $\{\tilde{x}_j^a(\{x_i\},\varphi_j,\psi)\}_{j=1,2,3}$ and $\{\tilde{x}_j^b(\{x_i\},\varphi_j,\psi)\}_{j=1,2,3}$. A crucial step in extending classical RG procedure to the quantum case is to follow the "classical" prescription to choose a *middle* out of three coefficients;

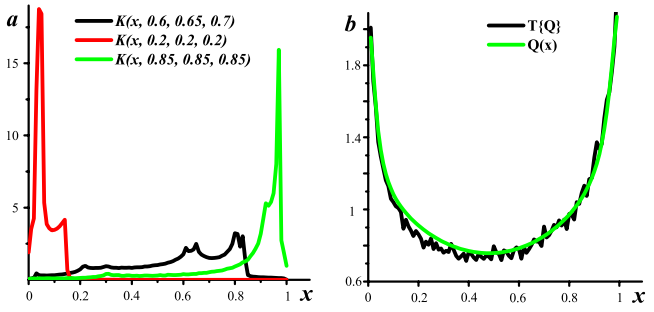

FIG. 6. (Color online) Left: kernel $K(x,x_1,x_2,x_3)$ is plotted from Eq. (19) for three sets (x_1,x_2,x_3). Right: approximate analytical solution (green line) of RG equation (21), given by Eq. (22), is plotted together with r.h.s. of Eq. (21), which is $T\{Q(x)\}$ (black line).

$$\tilde{x}^a[(x_i),(\varphi_i),\psi] = \mathrm{Mid}\{\tilde{x}_1^a[(x_i),\varphi_1,\psi],\tilde{x}_2^a[(x_i),\varphi_2,\psi],\tilde{x}_3^a[(x_i),\varphi_3,\psi]\} \tag{18}$$

and the same for $\tilde{x}^b(\{x_i\},\{\varphi_i\},\psi)$. Equation (18) is a quantum generalization of the classical equation (11). Note that selection of middle value in Eq. (18) is performed for *given* values of random phases, φ_1, φ_2, φ_3, and ψ. Within RG procedure different phases are uncorrelated, and in evaluation of the kernel we average over each of four phases independently. Finally, taking into account that contractions a and b are statistically equivalent, the expression for $K(x,\{x_i\})$ acquires the form

$$K[x,(x_i)] = \frac{1}{2}\langle \delta\{x - \tilde{x}^a[(x_i),(\varphi_i),\psi]\}\rangle_{\{\varphi_i,\psi\}} + \frac{1}{2}\langle \delta\{x - \tilde{x}^b[(x_i),(\varphi_i),\psi]\}\rangle_{\{\varphi_i,\psi\}}. \tag{19}$$

Quantum delocalization corresponds to the fixed point of transformation (15). It is found in Sec. V.

V. NUMERICAL RESULTS FOR FIXED POINT AND CRITICAL EXPONENT

A. Kernel

The examples of the kernel, $K(x)$, calculated using MATHEMATICA from Eqs. (16)–(19) are plotted in Fig. 6 for different sets x_1, x_2, and x_3. It is seen that the kernel supports the attractive critical points $x_1=x_2=x_3=0$ and $x_1=x_2=x_3=1$. Indeed, for values of $x_1=x_2=x_3=0.2$, the kernel is centered at even smaller value of $x \approx 0.04$, while for $x_1=x_2=x_3=0.85$ it is around bigger value of $x \approx 0.95$. In both cases the kernel is narrow. This is because for classical transmission coefficients interference does not play a role so that the phases drop out from Eqs. (16) and (17). However, for intermediate values $x_1=0.6$, $x_2=0.65$, and $x_3=0.7$ the kernel extends over entire interval $0<x<1$. It also exhibits peaks at $x=0.03$, 0.61, 0.65, 0.8, and 0.83. The origin of these peaks is the anomalous contributions of phases $\varphi_0=0,\pi$ and $\psi_0=0,\pi$ to the kernel. Indeed, for these values of phases we have $\partial\tilde{x}^{a,b}/\partial\varphi = \partial\tilde{x}^{a,b}/\partial\psi=0$ so that

$$\tilde{x}^{a,b}(\varphi,\psi) = \tilde{x}^{a,b}(\varphi_0,\psi_0) + \left.\frac{\partial_\varphi^2 \tilde{x}^{a,b}}{2}\right|_{\varphi_0,\psi_0} (\varphi-\varphi_0)^2 + \left.\frac{\partial_\psi^2 \tilde{x}^{a,b}}{2}\right|_{\varphi_0,\psi_0} (\psi-\psi_0)^2 + \partial_{\varphi\psi}^2 \tilde{x}^{a,b}|_{\varphi_0,\psi_0}(\varphi-\varphi_0)(\psi-\psi_0). \quad (20)$$

It is easy to check that, when the quadratic form of second derivatives is *negatively defined*, the corresponding contribution to the kernel is $\propto \ln|x-\tilde{x}^{a,b}(\varphi_0,\psi_0)|$. Therefore, the peaks in the kernel reflect the fact that two loops corresponding to phases ϕ and ψ are insufficient for complete averaging. Still, the phase volume of the singular contributions is small so that the fixed point of transformation (15) is not sensitive to these singularities.

B. Fixed point

The fixed point, $Q(x)$, of quantum RG equation (15), satisfies the following nonlinear integral equation:

$$Q(x) = T[Q(x)] = \int \left[\prod_{j=1}^{3} dx_j Q(x_j)\right] K(x,x_1,x_2,x_3), \quad (21)$$

which we have solved using MATHEMATICA. Starting from initial distribution, $Q(x)=1$, and performing analytical fit at each step of successive approximations, the following expression for the fixed point was obtained after the fourth step:

$$Q(x) = \frac{0.9}{1+10^3 x^2} + \frac{0.9}{1+5\cdot 10^2 (1-x)^2} + 0.63x^3 + 0.55(1-x)^3 + 0.6. \quad (22)$$

This expression is plotted in Fig. 6(b) with a green line. One can judge on the accuracy of approximate solution (22) by substituting it into the right-hand side of Eq. (21). The result, black line in Fig. 6(b), is indeed very close to Eq. (22).

The fixed point solution rises upon approaching $x=0$ and $x=1$. This behavior is inherited from the classical percolation. Note that similar behavior was found in Refs. 23 and 25 for the fixed point of the quantum bond percolation on the square lattice. Direct comparison with conductance distribution $P(G)$ found in Refs. 23 and 25 can be performed using the relation $P(G)=Q(\sqrt{G})/2\sqrt{G}$. This comparison indicates that, while numerically the fixed point distributions are close, Eq. (22) favors small values of x. Qualitatively, this reflects the fact that at critical energy, $\varepsilon=0$, electron incident along i_1 (see Fig. 4) is more likely to proceed along a_1 rather than switch to o_2. The asymmetry is seen more clearly if one interprets $Q(x)$ in terms of distribution and $\tilde{Q}$ of heights of the effective saddle point. This height is determined by the relation $x^2=1/(e^z+1)$ so that

$$\tilde{Q}(z) = \frac{e^z}{2(e^z+1)^{3/2}} Q([e^z+1]^{-1/2}). \quad (23)$$

The distribution $\tilde{Q}(z)$ is shown in Fig. 7 with a black line. It has an asymmetry toward large z.

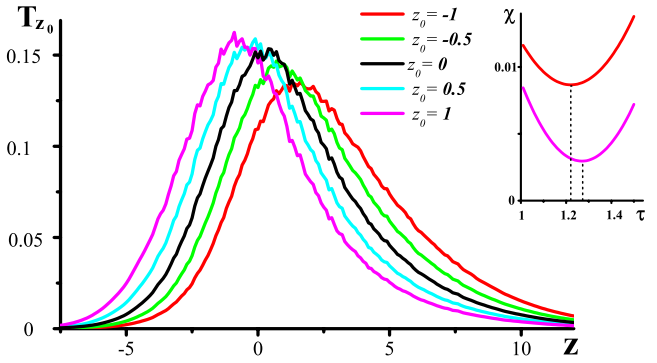

FIG. 7. (Color online) $T_{z_0}=T\{\tilde{Q}(z-z_0)\}$ is plotted for different z_0. Inset shows the variance, $\chi(\tau)$, plotted from Eq. (26). The minima correspond to $\tau=1.27$ and $\tau=1.22$ for $z_0=1$ and $z_0=-1$, respectively.

C. Critical exponent

To estimate the critical exponent, ν, which governs the divergence of localization radius, $\xi(\varepsilon)\propto 1/\varepsilon^\nu$, as a function of energy, ε, we used the reasoning from Refs. 23 and 25. Electron with finite energy, $\varepsilon \ll \Gamma$, "sees" the shifted distribution of the saddle point heights $\tilde{Q}(z-z_0)$, where $z_0 \ll 1$ is proportional to ε. The key step of the reasoning[23,25] is that, upon the RG transformation, the electron travels on the lattice with the lattice constant $\sqrt{3}$ and sees the shifted distribution of heights, $T\{\tilde{Q}(z-z_0)\}=\tilde{Q}(z-\tau z_0)$, where τ is some constant independent of z_0. After subsequent n RG steps this distribution evolves into $\tilde{Q}(z-\tau^n z_0)$. When the shift accumulates to reach ~ 1, the electron becomes localized within the size of a unit cell of renormalized lattice. Then from the relations

$$\xi(z_0) \propto \frac{1}{z_0^\nu}, \quad \xi=(\sqrt{3})^n, \quad z_0\tau^n \sim 1, \quad (24)$$

we find

$$\nu = \frac{\ln\sqrt{3}}{\ln \tau}. \quad (25)$$

This definition of ν is a quantum generalization of Eq. (10). In Fig. 7 the result of calculation $T\{\tilde{Q}(z-z_0)\}$ for four $z_0=-1$, -0.5, 0.5, and 1 is shown. We see that for these z_0 the shape of $T\{\tilde{Q}\}$ is only slightly affected by the shift. The curves are approximately equidistant so that an estimate of τ can be obtained simply from the horizontal separation of ≈ 0.4 between the neighboring curves. This yields $\tau \approx 1.25$ and, correspondingly, $\nu \approx 2.46$. For more accurate estimate we studied the variance

$$\chi(\tau,z_0) = \sum_{z_i} [T\{\tilde{Q}(z_i-z_0)\} - \tilde{Q}(z_i-\tau z_0)]^2 \quad (26)$$

as a function of τ for different values of the "energy shift" z_0. The sum [Eq. (26)] was taken over discrete set $z_i=-10+0.01i$ for $i=1,2,..,220$. In Fig. 7 we plot the variance for $z_0=1$ and $z_0=-1$. Both curves have pronounced minima at $\tau=1.27$ and 1.22, respectively. This translates into the values

of $\nu=2.3$ and $\nu=2.76$. Although these values are in good agreement with known value of ν, the accuracy of the above estimate is limited. The limitation is due to the fact that for $z_0=\pm 1$ the heights of maxima of the curves $T\{\tilde{Q}(z-z_0)\}$, shown in Fig. 7, differ from the height of $\tilde{Q}(z)$. This deviation would not be a problem for smaller z_0. However for $z_0=\pm 0.5$ the variance becomes small, and its dependence on τ becomes weak. Apparently, the variance [Eq. (26)] is affected by the wiggles at the top of the curves $T\{\tilde{Q}(z-z_0)\}$ that are much stronger for $z_0=\pm 0.5$ than for $z_0=\pm 1$, which makes the evaluation of χ for small z_0 ineffective.

VI. CONCLUSION

It is interesting to point out that while the classical limit of the Chalker-Coddington model based on potential (2) reduces to the bond percolation, similar form of potential (8) leads to the site percolation. The reason is the symmetry of corresponding potentials. As seen from Fig. 2, the hexagons surrounding the nodes of potential (8) have common *sides*. On the other hand, the squares, drawn around the nodes of potential (2), share the *vertices*.

Both the bond percolation on a square lattice and the site percolation on triangular lattice have $p_c=1/2$, which is ensured by self-duality. The RG descriptions[22] of both cases, having fixed point, $p_c=1/2$, effectively preserve this self-duality. As a result, the RG values for classical exponent come out close to $\nu=4/3$ in both RG schemes. In this paper we demonstrated that quantum extension of classical RG to the triangular lattice also yields the critical exponent close to the known value of $\nu=2.33$.

The fact that the simple RG scheme, considered in the present paper, describes the quantum Hall transition so accurately has a deep underlying reason. Delocalized state in the quantum Hall transition emerges as a result of competition of two trends: (i) quantum interference processes that survive in the presence of magnetic field (Hikami boxes, Ref. 29) tend to localize electron, while (ii) classical Lorentz force, by causing electron drift, prevents it from repeating closed diffusive trajectories. Both trends are incorporated into our RG scheme. Obviously, chiral motion is the consequence of the Lorentz force. Hikami boxes, on the other hand, are represented in the RG step in the form of *figure-eight* trajectories, as illustrated in Fig. 5. Note finally that simplicity of the RG description proposed here suggests possibility to extend it to different from quantum Hall universality classes (see, e.g., Refs. 30–33).

ACKNOWLEDGMENTS

We are grateful to I. Gruzberg and V. Kagalovsky for numerous discussions of the network models. This work was supported by the BSF under Grant No. 2006201.

APPENDIX A

Here we elaborate on the mapping of the problem of percolation over equipotential lines in the random potential [Eq. (8)] and the conventional site-percolation problem. The easiest way to establish this mapping is to surround all sites of triangular lattice with hexagons, as shown in Fig. 2. If the site is occupied, then the hexagon is, say, black; if the site is vacant, it is white. The distinctive property of the triangular lattice is that, when two hexagons touch, they automatically have a common side. Note in passing that this is not the case for a square lattice, where two squares, drawn around the sites, may touch by sharing a vertex but not share a side. In the site-percolation problem, the bond between two neighboring sites conducts if both of them are occupied. The same is to say that conduction is possible between two touching hexagons if they are both black. Percolation threshold corresponds to the portion of black hexagons when conduction over entire sample becomes possible. The fact that $p_c=1/2$ is a direct consequence of geometrical arrangement of hexagons due to which percolation over black hexagons rules out the percolation over white hexagons. Also, due to this arrangement, one of the colors always percolates.

Consider now potential (8). Black sites are now those in which $V_0<\varepsilon$. Configuration of equipotentials around this site is the rightmost of three shown in Fig. 1(b). Accordingly, configuration of equipotentials around the site with $V_0>\varepsilon$ is the leftmost of three shown in Fig. 1(b). Consider now two neighboring sites with $V_0<\varepsilon$. Figure 2 makes it apparent that any two black points inside hexagons surrounding these sites are connected via black color. Thus, it terms of connectivity over black, two neighboring sites with $V_0<\varepsilon$ are completely similar to two neighboring black hexagons. Similarly, as can be seen from Fig. 2, for two neighboring sites with $V_0<\varepsilon$ and $V_0>\varepsilon$, the centers of surrounding hexagons are disconnected. The same is true for two neighboring hexagons of opposite colors in the percolation problem. To complete the mapping, we note that, in percolation problem, the connectivity of two neighboring hexagons depends *entirely* on their colors; i.e., it does not depend on the color of the other neighbors. In the same way, in the problem of equipotentials, whether or not two neighboring sites are connected is determined exclusively by the signs of $V_0-\varepsilon$ in these sites.

APPENDIX B

The form of the S matrix [Eq. (13)] can be established with the help of Fig. 4. Matrix S relates the incident (i_1, i_2, and i_c) and outgoing (o_1, o_2, and o_c) amplitudes via transmission coefficients, x_1, x_2, and x_c. Form (13) follows from the system of six equations, which include also the amplitudes a_1, a_2, and a_c between the points of close contact of corresponding equipotentials. As seen from Fig. 4 the amplitudes a_1 and a_2 are related via x_1 as

$$a_1 = x_1 a_2 e^{i\phi_2} + y_1 i_1,$$

$$o_2 = -y_1 a_2 e^{i\phi_2} + x_1 i_1. \tag{B1}$$

Amplitudes a_c and a_1 are related via x_c,

$$a_c = x_c a_1 e^{i\phi_1} + y_c i_c,$$

$$o_1 = -y_c a_1 e^{i\phi_1} + x_c i_c. \tag{B2}$$

Finally, amplitudes a_2 and a_c are related via x_2,

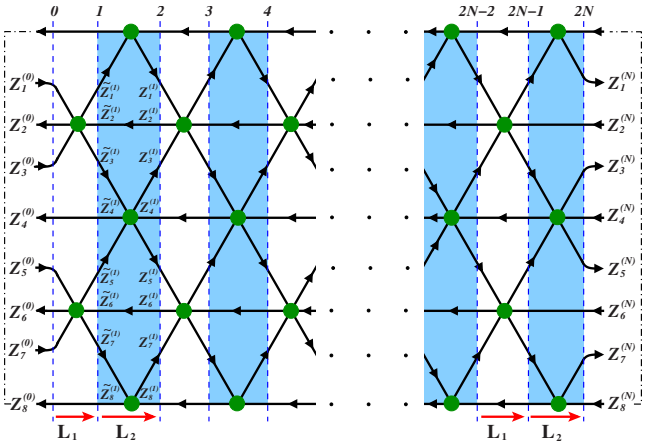

FIG. 8. (Color online) A slice of a network [Fig. 3] of width $M=8$ is shown. Three amplitudes on the links to left of green dot are related to three amplitudes to the right of green dot via matrix $\mathbf{X}$. The upper and the lower boundaries of the slice are connected by dashed-dotted lines manifesting that the amplitudes on these boundaries are the same by virtue of cyclic boundary conditions. Upon passing the white stripe, the vector of the amplitudes $\{Z_i\}$ is multiplied by the matrix $\mathbf{L}_1$. Upon passing the blue stripe the vector $\{\tilde{Z}_i\}$ is multiplied by $\mathbf{L}_2$.

$$a_2 = x_2 a_c e^{i\phi_c} + y_2 i_2,$$

$$o_c = -y_2 a_c e^{i\phi_c} + x_2 i_2. \tag{B3}$$

In Eqs. (B1)–(B3), phases ϕ_1, ϕ_2, and ϕ_c are the Aharonov-Bohm phases accumulated, respectively, by waves a_1, a_2, and a_c between the points of closed contact. Excluding a_1, a_2, and a_c from Eqs. (B1)–(B3) we recover S matrix (13) in which x_3 stands for x_c and ϕ_3 for ϕ_c.

In order to derive Eq. (16) we set in Eqs. (B1)–(B3) $i_2 = o_2 e^{i\varphi_2}$, as enforced by a contraction in Fig. 5(a). Upon setting $i_1=0$, we find the proportionality coefficient between o_1 and i_c. This recovers Eq. (16) in which $\varphi=\varphi_2+\phi_2$. Similarly, Eq. (17) is recovered upon setting $i_1=o_2 e^{i\varphi}$, as shown in Fig. 5(b), and relating the amplitudes o_1 and i_c.

APPENDIX C

In this Appendix we illustrate the transfer-matrix method in application to the network model on triangular lattice. Consider, by analogy to Ref. 6, a slice of length, N, shown in Fig. 8. It contains $M=8$ incident links, $Z_i^{(0)}$, and 8 outgoing links, $Z_i^{(N)}$. In general, the number of links must be $M=4m$, where m is integer. The slice shown in Fig. 8 can be obtained from the general network (Fig. 3) by two vertical cuts through the centers of triangles. The bottom links $Z_8^{(0)}$ and $Z_8^{(N)}$ in Fig. 8 are connected to the corresponding top links by dashed lines, reflecting the fact that these links must be identified with each other in order to impose a periodic boundary condition (Ref. 6). Scattering of waves at each node is described by the matrix $S=S_\Delta$ [Eq. (7)], which relates the amplitudes (o_1,o_2,o_3) to (i_1,i_2,i_3). To adapt $S=S_\Delta$ to the transfer-matrix algorithm, one has to recast Eq. (12) into the form

$$\begin{pmatrix} o_2 \\ i_2 \\ o_3 \end{pmatrix} = \mathbf{X} \begin{pmatrix} i_1 \\ o_1 \\ i_3 \end{pmatrix}, \tag{C1}$$

which connects the amplitudes to the left and to the right from the node. Direct calculation yields the following form of matrix $\mathbf{X}$ in terms of elements, s_{ij} of S_Δ.

$$\mathbf{X} = \begin{pmatrix} \left[s_{21} - \frac{s_{11}s_{22}}{s_{12}}\right] & \frac{s_{22}}{s_{12}} & \left[s_{23} - \frac{s_{22}s_{13}}{s_{12}}\right] \\ -\frac{s_{11}}{s_{12}} & \frac{1}{s_{12}} & -\frac{s_{13}}{s_{12}} \\ \left[s_{31} - \frac{s_{11}s_{32}}{s_{12}}\right] & \frac{s_{32}}{s_{12}} & \left[s_{33} - \frac{s_{32}s_{13}}{s_{12}}\right] \end{pmatrix}. \tag{C2}$$

For energies close to the critical $\varepsilon=0$, the S matrix is given by Eq. (7); $S=S_\Delta$. Making use of Eq. (7), it is straightforward to find the energy dependence of $\mathbf{X}$:

$$\mathbf{X} = \begin{pmatrix} 2(1+\varepsilon) & -2(1+\varepsilon) & 1 \\ 2(1+\varepsilon) & -3 & 2(1-\varepsilon) \\ 1 & -2(1-\varepsilon) & 2(1-\varepsilon) \end{pmatrix}. \tag{C3}$$

Operators $\mathbf{L}_1$ and $\mathbf{L}_2$ act in white and "blue" stripes, respectively. Operator $\mathbf{L}_1$ performs the transformation of the vector of amplitudes $\{Z_i^{(n)}\}$ into $\{\tilde{Z}_i^{(n+1)}\}$, while $\mathbf{L}_2$ performs the transformation of $\{\tilde{Z}_i^{(n)}\}$ into $\{Z_i^{(n)}\}$. Matrix forms of $\mathbf{L}_1$ and $\mathbf{L}_2$ in terms of elements of matrix, $\mathbf{X}$, are the following:

$$\mathbf{L}_1 = \begin{pmatrix} x_{11} & x_{12} & x_{13} & 0 & \cdot & \cdot & \cdot & \cdot \\ x_{21} & x_{22} & x_{23} & 0 & \cdot & \cdot & \cdot & \cdot \\ x_{31} & x_{32} & x_{33} & 0 & \cdot & \cdot & \cdot & \cdot \\ 0 & 0 & 0 & 1 & \cdot & \cdot & \cdot & \cdot \\ \cdot & \cdot & \cdot & \cdot & x_{11} & x_{12} & x_{13} & 0 \\ \cdot & \cdot & \cdot & \cdot & x_{21} & x_{22} & x_{23} & 0 \\ \cdot & \cdot & \cdot & \cdot & x_{31} & x_{32} & x_{33} & 0 \\ \cdot & \cdot & \cdot & \cdot & 0 & 0 & 0 & 1 \end{pmatrix}, \tag{C4}$$

$$\mathbf{L}_2 = \begin{pmatrix} x_{33} & 0 & \cdot & \cdot & \cdot & \cdot & x_{31} & x_{32} \\ 0 & 1 & \cdot & \cdot & \cdot & \cdot & 0 & 0 \\ \cdot & \cdot & x_{11} & x_{12} & x_{13} & 0 & \cdot & \cdot \\ \cdot & \cdot & x_{21} & x_{22} & x_{23} & 0 & \cdot & \cdot \\ \cdot & \cdot & x_{31} & x_{32} & x_{33} & 0 & \cdot & \cdot \\ \cdot & \cdot & 0 & 0 & 0 & 1 & \cdot & \cdot \\ x_{13} & 0 & \cdot & \cdot & \cdot & \cdot & x_{11} & x_{12} \\ x_{23} & 0 & \cdot & \cdot & \cdot & \cdot & x_{21} & x_{22} \end{pmatrix}, \tag{C5}$$

with dots standing for zeroes. Specific form of $\mathbf{L}_2$ accounts for the cyclic boundary conditions in the vertical direction.

In addition to the scattering at the nodes (green dots in Fig. 8), propagation along the network links accumulates random phases. If we denote the phases on the links crossing vertical lines $2n$ by $\varphi_i^{(n)}$ and those crossing lines $2n+1$ by $\psi_i^{(n)}$, then all the random phases at the links can be taken into account by introducing diagonal phase matrices

$$\mathbf{P}_1^{(n)} = \mathrm{diag}\{e^{i\varphi_1^{(n)}}, \cdots, e^{i\varphi_8^{(n)}}\} \tag{C6}$$

and

$$\mathbf{P}_2^{(n)} = \mathrm{diag}\{e^{i\psi_1^{(n)}}, \cdots, e^{i\psi_8^{(n)}}\}. \tag{C7}$$

Finally, the transfer matrix, $\mathbf{T}$, of the slice Fig. 8 is given by the product

$$\mathbf{T} = \prod_{n=N-1}^{0} \mathbf{L}_2\mathbf{P}_2^{(n)}\mathbf{L}_1\mathbf{P}_1^{(n)}, \tag{C8}$$

which runs in the reverse order. This product is completely analogous to the transfer matrix of the slice in the Chalker-Coddington model.

[1] B. Shapiro, Phys. Rev. Lett. **48**, 823 (1982).
[2] A. Altland and M. R. Zirnbauer, Phys. Rev. B **55**, 1142 (1997).
[3] R. Merkt, M. Janssen, and B. Huckestein, Phys. Rev. B **58**, 4394 (1998).
[4] J. Cardy, Commun. Math. Phys. **258**, 87 (2005).
[5] B. Kramer, T. Ohtsuki, and S. Kettemann, Phys. Rep. **417**, 211 (2005).
[6] J. T. Chalker and P. D. Coddington, J. Phys. C **21**, 2665 (1988).
[7] A. MacKinnon and B. Kramer, Phys. Rev. Lett. **47**, 1546 (1981).
[8] D.-H. Lee, Z. Wang, and S. Kivelson, Phys. Rev. Lett. **70**, 4130 (1993).
[9] D. K. K. Lee and J. T. Chalker, Phys. Rev. Lett. **72**, 1510 (1994).
[10] D. K. K. Lee, J. T. Chalker, and D. Y. K. Ko, Phys. Rev. B **50**, 5272 (1994).
[11] Z. Wang, D.-H. Lee, and X.-G. Wen, Phys. Rev. Lett. **72**, 2454 (1994).
[12] I. M. Ruzin and S. Feng, Phys. Rev. Lett. **74**, 154 (1995).
[13] V. Kagalovsky, B. Horovitz, and Y. Avishai, Phys. Rev. B **52**, R17044 (1995).
[14] V. Kagalovsky, B. Horovitz, and Y. Avishai, Phys. Rev. B **55**, 7761 (1997).
[15] Z. Wang, B. Jovanović, and D.-H. Lee, Phys. Rev. Lett. **77**, 4426 (1996).
[16] S. Cho and M. P. A. Fisher, Phys. Rev. B **55**, 1637 (1997).
[17] R. Klesse and M. Metzler, Phys. Rev. Lett. **79**, 721 (1997).
[18] M. Janssen, M. Metzler, and M. R. Zirnbauer, Phys. Rev. B **59**, 15836 (1999).
[19] L. P. Pryadko and A. Auerbach, Phys. Rev. Lett. **82**, 1253 (1999).
[20] R. Klesse and M. R. Zirnbauer, Phys. Rev. Lett. **86**, 2094 (2001).
[21] R. A. Römer and P. Cain, Adv. Solid State Phys. **42**, 237 (2003); Int. J. Mod. Phys. B **19**, 2085 (2005); E. Shimshoni, Mod. Phys. Lett. B **18**, 923 (2004).
[22] P. J. Reynolds, W. Klein, and H. E. Stanley, J. Phys. C **10**, L167 (1977).
[23] A. G. Galstyan and M. E. Raikh, Phys. Rev. B **56**, 1422 (1997).
[24] D. P. Arovas, M. Janssen, and B. Shapiro, Phys. Rev. B **56**, 4751 (1997).
[25] P. Cain, R. A. Römer, M. Schreiber, and M. E. Raikh, Phys. Rev. B **64**, 235326 (2001).
[26] P. Cain, R. A. Römer, and M. E. Raikh, Phys. Rev. B **67**, 075307 (2003).
[27] U. Zülicke and E. Shimshoni, Phys. Rev. B **63**, 241301(R) (2001).
[28] M. F. Sykes and J. W. Essam, Phys. Rev. Lett. **10**, 3 (1963).
[29] S. Hikami, Phys. Rev. B **24**, 2671 (1981).
[30] V. Kagalovsky, B. Horovitz, Y. Avishai, and J. T. Chalker, Phys. Rev. Lett. **82**, 3516 (1999).
[31] T. Senthil, J. B. Marston, and M. P. A. Fisher, Phys. Rev. B **60**, 4245 (1999).
[32] I. A. Gruzberg, A. W. W. Ludwig, and N. Read, Phys. Rev. Lett. **82**, 4524 (1999).
[33] E. J. Beamond, J. Cardy, and J. T. Chalker, Phys. Rev. B **65**, 214301 (2002).